

Using the material point method to model chemical/mechanical coupling in the deformation of a silicon anode

Chris Gritton¹, James Guilkey², Justin Hooper³, Dmitry Bedrov³,
Robert M. Kirby¹, Martin Berzins¹

¹Scientific Computing and Imaging Institute, University of Utah

²Department of Mechanical Engineering, University of Utah

³Department of Materials Science and Engineering, University of Utah

May 26, 2017

Abstract

The lithiation and delithiation of a silicon battery anode is modeled using the material point method (MPM). The main challenges in modelling this process using the MPM is to simulate stress dependent diffusion coupled with concentration dependent stress within a material that undergoes large deformations. MPM is chosen as the numerical method of choice because of its ability to handle large deformations. A method for modelling diffusion within MPM is described. A stress dependent model for diffusivity and three different constitutive models that fully couple the equations for stress with the equations for diffusion are considered. Verifications tests for the accuracy of the numerical implementations of the models and validation tests with experimental results show the accuracy of the approach. The application of the fully coupled stress diffusion model implemented in MPM is applied to modelling the lithiation and delithiation of silicon nanopillars.

1 Introduction

Electrochemical storage devices are becoming pervasive in today's society. Electronic devices ranging from smart phones to electric vehicles all depend on efficient, robust, and high-capacity electrochemical storage. Driven by this demand for greater energy storage capacity, new materials are being sought to improve the performance of batteries. One promising material that is currently being explored to improve performance is silicon. Silicon has a theoretical charge capacity in the range of 3500 mAhg^{-1} to 4200 mAhg^{-1} [1, 2] which is 10 times larger than that of current anode materials such as graphite at 350 mAhg^{-1} [3]. The large theoretical charge capacity comes from silicon's ability to accommodate multiple lithium ions per silicon atom. As a silicon anode approaches full lithiation, the ratio of lithium ions to silicon atoms is 3.75 to 1 [4]. This ratio of lithium ions to silicon leads to a large volume change of up to $\sim 280\%$ [5]. This large change in volume over multiple charge/discharge cycles can lead to mechanical failures that decrease the charge capacity and thus reducing the effectiveness of using silicon as an anode material.

A key observable trait of the lithiation process is the notable lithiation front that occurs as lithium ions diffuse through the silicon material. Experimental results presented by Wang et al. [5] show that as lithium diffuses through the silicon material, there exists a sharp phase transition between the lithiated silicon and the pure amorphous silicon. This sharp phase transition produces large strains on the lithium rich side of the phase transition. Wang et al. [5] report strains in the range of 160% in the region around the phase transition which produce a large percentage of the total volume expansion. The normalized concentration of lithium in the region of the phase transition is approximately 67% or 2.5 lithiums to 1 silicon [5]. Outside

of the region of the phase transition, the concentrations gradients for lithium are relatively small in the lithiated regions the lithiation front.

By gaining an understanding of the chemical and mechanical changes that occur during the lithiation and delithiation phases of a charge cycle, new anode configurations and geometries can be explored that reduce the mechanical failure points within an anode. Numerous physical experiments have been performed testing different anode configurations, ranging from thin films [6], to nano pillars [7], to honeycomb structures [8]. Through the use of computational simulations new anode configurations can be explored more easily which can lead to better insights into the configurations used in physical experiments.

The study of diffusion-induced stress can be found in work dating back to the 1960's. Prussin [9] formulated a model that couples the diffusion of a solute in a single-crystal silicon wafer to the generation of stresses and the resultant crystal dislocation distributions. The work by Li et al. [10] involved the derivation of models for the chemical potentials of both the mobile guest species and immobile host material where the host material is in a stressed state. Beginning in the 1970's Larché and Cahn [11, 12, 13, 14] developed a framework for modelling diffusion induced stress. The model uses a theoretical embedded network within a material to track deformations. The diffusion process is driven by the chemical potential of the guest species within the host material. The derived chemical potential is a function of both the guest species concentration and hydrostatic stress. The work of Larché and Cahn now forms the basis for much of the current research being done to model the lithiation of silicon anodes [15, 16, 4].

Alternatives to the Larché and Cahn model for diffusion induced stress have also been proposed. For example in the paper by Wu [17] the argument is made that the Eshelby stress tensor should be used in the stress dependent chemical potential as opposed to the hydrostatic Cauchy stress. Cui et al. [18] extends the work of Wu to applications in modelling the stress-dependent chemical potential of lithium ion batteries. Other methods avoid the derivation of a chemical potential and instead derive an empirically based model for the diffusion process [5, 19, 20, 21].

As there have been multiple models proposed for the lithiation of a silicon anode, there have also been multiple methods used to simulate the lithiation/delithiation process. One method has been to reduce the dimensionality of the problem to a spherical geometry for the anode [22, 23]. While the reduction of dimensionality can lead to insights into the lithiation/delithiation process without the higher computational costs of higher dimensional simulations, key features associated with anode geometries will be lost. For numerical simulations that cannot be reduced to one dimension the Finite Element Method (FEM) has been a popular choice. A large number of the published simulations involving the lithiation process of silicon have been done using the finite element method [24, 25, 5, 19, 26]. FEM is well understood and there exists a large number of different code bases, both commercial and open sourced, upon which a researcher can draw.

Key experimental observations of a silicon anode undergoing the lithiation process show the large deformations that it will experience. A variety of numerical methods have been used to model large deformations. Mesh based methods such as FEM [27] and XFEM [28] have found success along with meshless methods such as SPH [29] and RPKM [30]. An alternative to these approaches that has been found to be successful in modeling large deformations is the Material Point Method (MPM) [31]. MPM uses aspects of both FEM and particle methods to carry out computations.

MPM along with the multiple variants of the method are well described in the literature [32, 33, 34, 35, 36, 37]. For the the purpose of this paper the Convected Particle Domain Interpolation (CPDI) variant, as described by Sadeghirad and Brannon [38], will be used. The MPM algorithm as described in [34, 38] has been implemented in the Uintah computational framework [39], and serves as the code base for this work. The *Uintah User Guide* [40] includes a further description of the MPM component, including additional feature that have been implemented therein. The primary contribution of this paper is the chemical-mechanical coupling, including the concentration diffusion solver working in concert with the momentum balance solver.

The paper proceeds as follows. Section 2 will be a brief overview of MPM followed by a description of the method used to model diffusion within MPM. Results from verification tests of the diffusion method will also be presented. Section 3 will be a description of the two way coupling of the chemical process of lithium diffusion and mechanical process of momentum balance. Section 4 will present simulation results along with a discussion of the issues and simulation outcomes associated with time integration, constitutive

model selection, boundary conditions, and parameter choices. Section 4.6 will look at the results of bonding an anode to a fixed or deformable substrate. Section 4.7 will present the simulation results of a silicon anode undergoing a full lithiation/delithiation cycle. Lastly, Section 5 will draw conclusions and discuss further work.

2 The Material Point Method

The Material Point Method was developed in the 1990s by Sulsky et al. [32] as numerical solution to the momentum balance equation,

$$\rho \mathbf{a} = \nabla \cdot \boldsymbol{\sigma} + \rho \mathbf{b}, \quad (1)$$

where ρ is density, \mathbf{a} is acceleration, $\boldsymbol{\sigma}$ is stress, and \mathbf{b} is the acceleration that comes as a result of an external force such as gravity. The basic premise of MPM is that the domain of an object is discretized into material points. Properties such as mass and momentum are assigned to each material point. The material points are Lagrangian in nature and are advected within the domain of the problem. The second component of MPM is a background Eulerian grid. Particle masses and momentums are mapped to the grid nodes using an appropriate choice of grid and particle basis functions. The grid is then used to solve the momentum balance equation. Particles values are updated by interpolating changes in the state from the grid nodes to the particles and then integrating forward in time. Variations in MPM come as a result of the choices made in grid and particle basis functions.

2.1 Modeling Diffusion in MPM

During the processes of lithiation and delithiation, lithium is transported by two different processes. The first process is that of advection which arises as a result of the deformation of the host material. As the host material undergoes deformation the guest material embedded in the material is carried along with the deforming host material. The modeling of this process comes as result of lithium being assigned to a material point, the mass of the host material of each material point does not change. The advection of the guest material is accounted for naturally when material points are advected.

The second form of transport for lithium ions comes in the form of diffusion. For the purposes of this paper, the lithium concentration is normalized, $c = c_g/c_{max}$, where c_{max} is the molar concentration representative of a ratio of 3.75 lithium to 1 silicon and c_g is the current molar concentration. Diffusion is modeled in MPM using many of the same numerical methods that are used in solving the momentum balance equations. The standard diffusion equation is,

$$\frac{\partial c}{\partial t} = -\nabla \cdot \mathbf{J}, \quad (2)$$

where \mathbf{J} is the normalized concentration flux. The equation for the normalized concentration flux is,

$$\mathbf{J} = -D\nabla c. \quad (3)$$

where D is the diffusivity constant.

Modeling diffusion in MPM is as follows. First, particle masses are mapped to the grid nodes,

$$m_i = \sum_p \varphi_{ip} m_p, \quad (4)$$

where m_i is the mass at the nodes, m_p is the mass at the particles, and φ_{ip} is the weighting function. For a general description of the use of the weighting function used in MPM the reader is referred to [37] and for a specific description of the weighting functions used in the CPDI variant of MPM see [38]. The mapping of masses from particles to grid nodes is also a step found in the MPM solution to the momentum balance equation and thus grid values for m_i have already been computed.

The second step is to map the normalized particle concentration values to grid nodes. This is done in a similar fashion to mapping velocity values from particles to grid nodes and is done as follows,

$$c_i = \frac{\sum_p \varphi_{ip} m_p c_p}{m_i}, \quad (5)$$

where c_i is the normalized grid concentration value and c_p is the normalized particle concentration value. The third step is to calculate the flux values at the particles. This is done by taking the gradient of the weighting function that interpolates normalized concentration values at the nodes to the particles,

$$\mathbf{J}_p = -D \sum_i \nabla \varphi_{ip} c_i. \quad (6)$$

The fourth step is to compute the divergence of the flux term. This is done in a manner similar to that used in computing the divergence of stress,

$$\frac{\partial c_i}{\partial t} = \frac{\sum_p (\mathbf{J}_p \cdot \nabla \varphi_{ip}) m_p}{m_i}. \quad (7)$$

The fifth step is to update normalized concentration values at the particles,

$$c_p^{n+1} = c_p^n + dt \sum_i \varphi_{ip} \frac{\partial c_i}{\partial t}. \quad (8)$$

This method of modeling concentration diffusion within MPM is similar to methods used previously in modeling heat diffusion [41, 42, 43].

2.2 Verification of MPM Diffusion

A one-dimensional system with an analytical solution is used to test the method described above. The test problem is defined with the initial and boundary conditions on the spatial domain $0 \leq x \leq 1$ with a discontinuity existing between the initial condition and the boundary conditions and is written as follows,

$$\frac{\partial c}{\partial t} = -\frac{\partial J}{\partial x}, \quad (9)$$

$$c(x, 0) = 0.0, \quad c(0, t) = 1.0, \quad c(1, t) = 0.0. \quad (10)$$

The flux term is defined as,

$$J = -D \frac{\partial c}{\partial x}, \quad (11)$$

where D is the diffusivity constant. Combining Equation (9) and Equation (11) produces the following equation,

$$\frac{\partial c}{\partial t} = D \frac{\partial^2 c}{\partial x^2}. \quad (12)$$

The solution to Equation (12), subject to the initial and boundary conditions given in Equation (10), is well known [44],

$$c(x, t) = (1 - x) - \frac{2}{\pi} \sum_{n=1}^{\infty} \frac{1}{n} e^{-D\pi^2 n^2 t} \sin(n\pi x). \quad (13)$$

For the purposes of determining the accuracy of the numerical method the first 1000 terms of the Fourier expansion should be sufficient.

The numerical solution to Equation (12) is found using the MPM diffusion method described above. The problem set-up is such that there are two particle per cell. A set of seven different simulations were run with grid spacings of 0.1, 0.05, 0.02, 0.01, 0.005, 0.002 and 0.001, with the data again being captured at

simulation time 0.25. The error for the method was calculated taking the L2 norm of the relative error in concentration,

$$e_p = \begin{cases} (c_p - \hat{c}_p)/c_p & \text{if } c_p \neq 0 \\ 0 & \text{if } c_p = 0 \end{cases} \quad (14)$$

$$\text{error} = \frac{\sqrt{\sum_{p=1}^N e_p^2}}{N}, \quad (15)$$

where e_p is the relative error, c_p is the true solution, and \hat{c}_p is the computed value at each particle p and N is the total number of particles. Figure 1.a shows a comparison of the actual results from the MPM diffusion solution with the true solution for a grid size of 0.02. Figure 1.b shows the convergence of the error as grid resolution increases. From the data it can be seen experimentally that the order of accuracy of the MPM method appears to be $O(h)$, for reference purposes the red line indicates a slope of 1.0 and the red error marker of Figure 1.b correlates with the results shown in Figure 1.a.

2.3 Advected Flux Boundary Conditions

In the calculations carried out here, a flux was applied to the surface of the object under investigation that was intended to mimic the flux induced by applying a voltage difference between the object and a far away cathode. Due to coupling between the concentration and mechanical state, increasing concentration results in deformation of the object. Hence, the location of the surface upon which the flux is prescribed is changing with time. For the simulations here, initial surface particles were identified, and the initial external area was computed and recorded. It was assumed here (and inspection of the results below validates this assumption), that while the surface moves and stretches, there is no change to what would be considered a surface particle, or to which face of the particle would be considered a surface. A current assumption that is probably less valid, and will be fixed in future work, is that the surface area associated with each particle remains constant. Inspection of the subsequent results show that this is not a valid assumption, but given the relatively uniform expansion of the object that we are currently interested in, this is similar to prescribing a slightly lower flux than intended. In future work, the particle area will be evolved according to the particle deformation gradient, which is already part of the particle data that is integrated in time.

A time varying flux is applied to the surface particles by computing the rate of change in concentration that this flux would be associated with, namely,

$$\left(\frac{\partial c_{pv}}{\partial t}\right)_{bc} = J(t)_{bc} \frac{A_p}{V_p}, \quad (16)$$

where $J(t)_{bc}$ is the user defined flux boundary condition, A_p is the surface of the particle upon which the boundary flux condition is being applied, V_p is the particle volume, and $(\partial c_{pv}/\partial t)_{bc}$ is the rate of change of concentration in the particle. Note that to avoid exceeding a normalized concentration of 1, a flux restriction factor is used, such that:

$$\left(\frac{\partial c_{pv}}{\partial t}\right)'_{bc} = \left(\frac{\partial c_{pv}}{\partial t}\right)_{bc} \cdot (1 + .25 \log(1 - c_p)). \quad (17)$$

Thus, once the concentration starts to saturate the substrate, the flux at that surface is gradually reduced. While the equation above is ad hoc, this reflects physically meaningful behavior. This rate of change is mapped to the grid and, in the case of boundary particles, functions as an additional source term in Equation 7,

$$\frac{\partial c_i}{\partial t} = \frac{\sum_p (\mathbf{J}_p \cdot \nabla \varphi_{ip}) m_p}{m_i} + \frac{\sum_p (\partial c_{pv}/\partial t)'_{bc} \varphi_{ip} m_p}{m_i}. \quad (18)$$

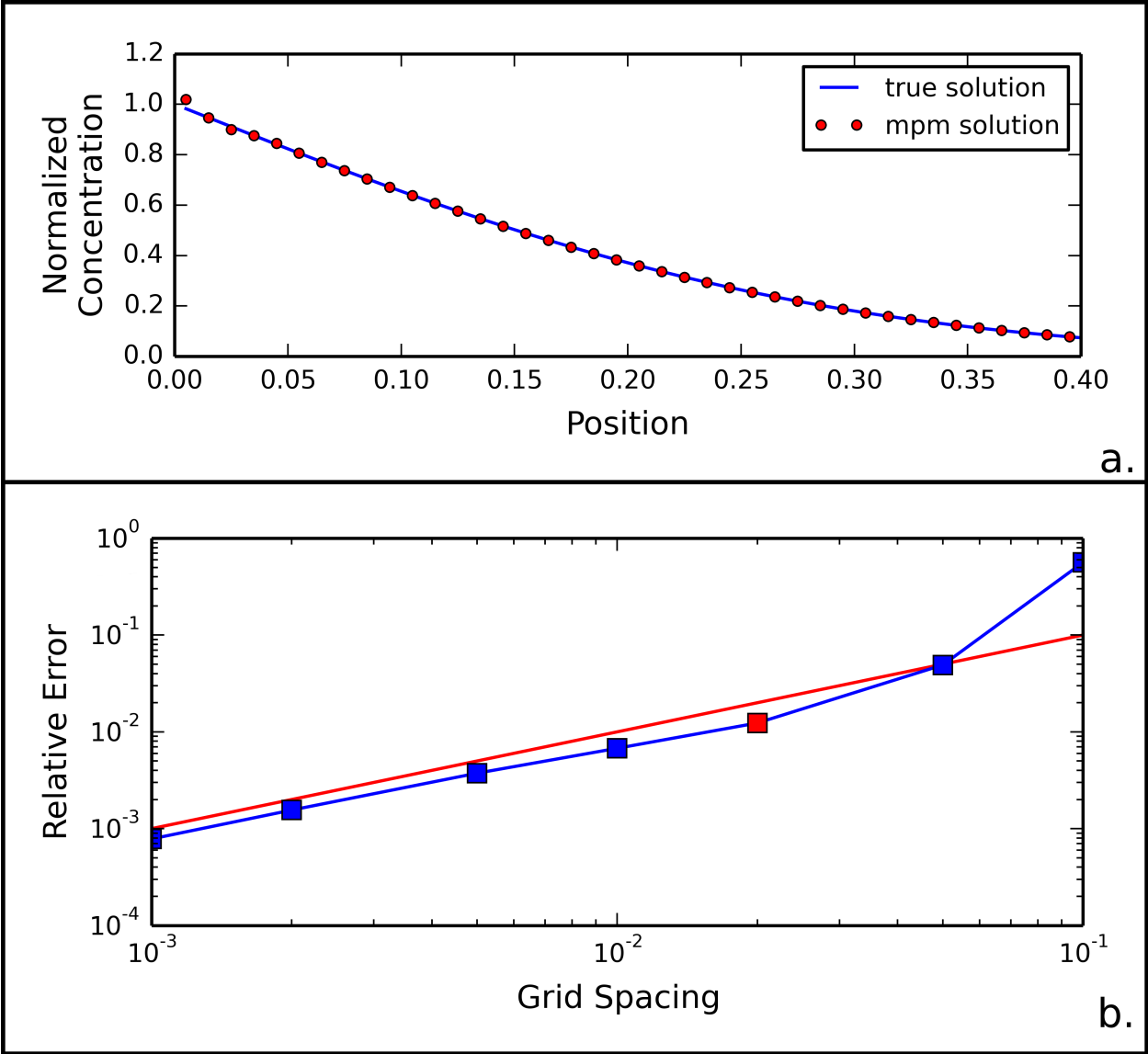


Figure 1: (a) shows the computed results from the MPM diffusion method compared against the true solution for grid size 0.02 and at time .25. (b) is the error convergence plot for the MPM diffusion method. The red marker correlates with the results shown in (a) and the red line is for reference purposes and is a slope of 1.0.

3 Chemical/Mechanical Coupling in MPM

3.1 Coupling Stress to Diffusion

Multiple models have been formulated that couple the affects of stress with the diffusion process [5, 23, 45, 46, 19, 20, 21]. The existing models can be broken up into two basic groups. The first group, [23, 45, 46], follows the framework that was developed by Larché and Cahn [11, 12, 13, 14] and computes the concentration flux based on a formulation of the chemical potential of lithium within the host silicon anode. The Larché and Cahn chemical potential is defined as,

$$\mu_{Li} = \mu_{Li}^0 + RT \ln \left(\gamma \frac{c}{1-c} \right) + \kappa \frac{d\epsilon_{vol}^c}{dc} p - \frac{\kappa}{2} B_{ijkl} \sigma_{ij} \sigma_{kl}, \quad (19)$$

where μ_{Li}^0 is the reference chemical potential, R is the ideal gas constant T is temperature, γ is the activation coefficient, κ is the molar volume of silicon, $\epsilon_{vol}^c = \epsilon_{ii}^c/3$ is the volumetric portion of the stress-free strain due to the insertion of lithium, $p = -\sigma_{ii}/3$, and $B_{ijkl} = dS_{ijkl}/dc$ is the rate of change of the elastic compliance tensor, S_{ijkl} , with respect to concentration. The flux based on the chemical potential is defined as,

$$\mathbf{J} = -D \frac{c}{RT} \nabla \mu. \quad (20)$$

If the constitutive model has compliance tensor that is not dependent upon concentration, as is the case for the model discussed below, then B_{ijkl} reduces to zero and in cases where the relationship between the stress-free strain, ϵ_{ij}^c , and concentration is linear then $d\epsilon_{vol}^c/dc$ is a constant. Based on the following two assumptions Equation 20 can be written as a combination of the concentration and pressure gradients,

$$\mathbf{J} = -\frac{D\gamma}{(1-c)} \nabla c - \frac{D\kappa c}{RT} \frac{d\epsilon_{vol}^c}{dc} \nabla p. \quad (21)$$

The second group, [5, 19, 20, 21], uses an empirical based approach where a model is formulated that takes as input concentration and in some cases stress and then the user adjusts a set of parameters to produce the desired behavior. In the empirical based approach flux is defined as follows,

$$\mathbf{J} = -D(c, \sigma) \nabla c. \quad (22)$$

While both methods can be implemented within the MPM diffusion framework described above, for the purposes of this paper the approach of the second group will be used. The selection of the empirical based approach is based upon the observation that the greatest changes in pressure occur in regions where lithium is diffusing into the non-lithiated amorphous silicon, in the areas behind this region the changes in pressure are minimal and the contribution of the pressure gradient to the concentration flux is small. The empirical based approach is able to approximate the behavior of the lithiation of non-lithiated amorphous silicon and provides a good first approximation of the diffusion process.

The normalized concentration and pressure dependent function for diffusivity that will be used for this paper is defined as,

$$D(c, p) = \begin{cases} D_0 e^{\alpha c} & \text{if } p \leq 0, \\ D_0 e^{\alpha c - \beta p} & \text{if } 0 < p < p_{max}, \\ D_0 e^{\alpha c - \beta p_{max}} & \text{if } p \geq p_{max}, \end{cases} \quad (23)$$

where D_0 is the initial diffusivity, α and β are tuning parameters, and p_{max} is the capped value for pressure. It is through the diffusivity function that stress is coupled to the diffusion process. By way of comparison, Berla et al. [21] and Wang et al. [20] use a cubic polynomial to compute diffusivity as solely function of concentration. The diffusivity function is defined as,

$$D(c) = D_0(1-c)^3 + D_{max}c^3, \quad (24)$$

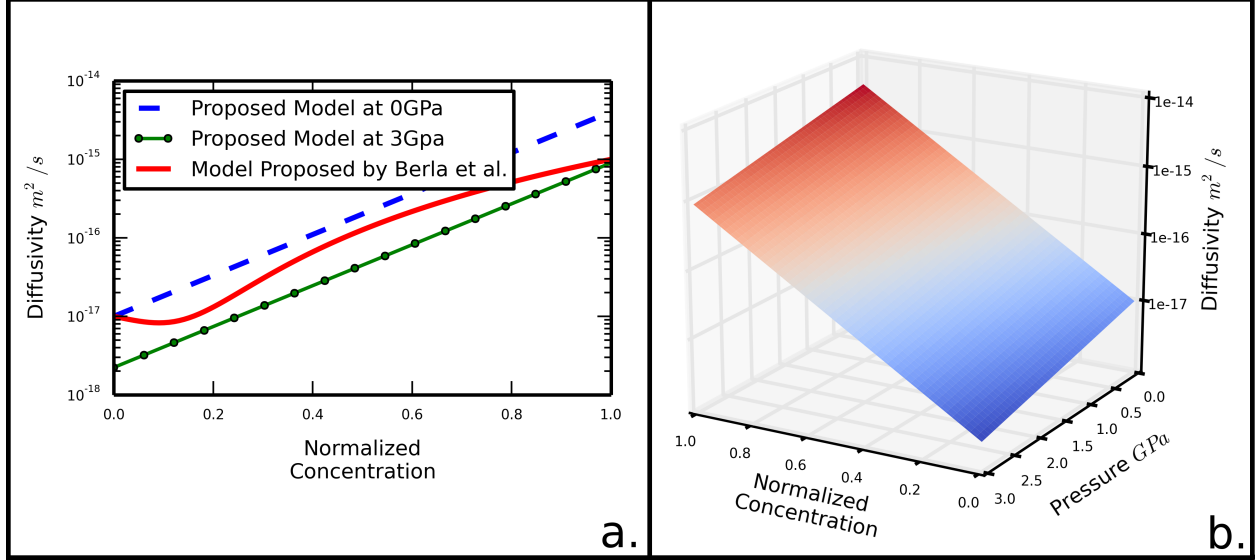


Figure 2: (a) Comparison of the diffusivity function evaluated at 0 GPa and 3 GPa compared against the diffusivity function proposed by Berla et al. (b) The surface plot of the diffusivity function over the range of $[0,1]$ for concentration and $[0,3]$ GPa for pressure.

where D_{max} is the diffusivity at full concentration. Using the following parameters $D_0 = 10^{-17} m^2/s$, $D_{max} = 10^{-15} m^2/s$, $\alpha = 6.0$, $\beta = .5$ and $p_{max} = 3$ GPa for Equation (23) and Equation (24) diffusivity curves were evaluated over the normalized concentration range $[0, 1]$. Figure 2.a shows the results for Equation (23) and Equation (24) with Equation (23) being evaluated at 0 GPa and 3 GPa. Figure 2.b shows the surface plot of Equation 23 over the normalized concentration range of $[0, 1]$ and the pressure range from $[0, 3]$ GPa with $\alpha = 6.0$, $\beta = .5$ and $p_{max} = 3$ GPa.

3.2 Coupling Concentration to Stress

The modeling of the silicon anode material response to concentration diffusion is done using a hypoelastic-plastic constitutive model. The hypoelastic-plastic model allows for an additive decomposition of the rate of strain tensor into elastic, plastic, and stress-free volumetric components,

$$\mathbf{d} = \mathbf{d}^e + \mathbf{d}^p + \mathbf{d}^c, \quad (25)$$

where \mathbf{d}^e is the elastic rate of strain, \mathbf{d}^p is the plastic rate of strain, and \mathbf{d}^c is the stress-free volumetric rate of strain due to the insertion of lithium into the silicon material.

Objectivity is maintained in the stress calculation by rotating stress and the rate of strain back to its unrotated state where the stress update calculation is then performed, and then subsequently this updated stress is rotated back to its previous state. This is done using the rotation tensor obtained from the polar decomposition of the deformation gradient,

$$\mathbf{F} = \mathbf{R}\mathbf{U}, \quad (26)$$

where \mathbf{F} is the deformation gradient, \mathbf{R} is the rotation tensor, and \mathbf{U} is the right stretch tensor. The transformation of stress from its rotated to unrotated state is performed as follows,

$$\bar{\boldsymbol{\sigma}} = \mathbf{R}^T \boldsymbol{\sigma} \mathbf{R}, \quad (27)$$

and the transformation for the rate of strain is done in like manner,

$$\bar{\mathbf{d}} = \mathbf{R}^T \mathbf{d} \mathbf{R}, \quad (28)$$

where the rate of strain is the symmetric part of the velocity gradient, \mathbf{l} ,

$$\mathbf{d} = \frac{1}{2}(\mathbf{l} + \mathbf{l}^T). \quad (29)$$

The unrotated symmetric part of the velocity gradient is chosen as a rate of strain because of the relatively low computational cost relative to other possible choices for rates of strain and under conditions where the rotation of the principle referential directions is small the unrotated symmetric part of the velocity gradient is a good approximation for Hencky strain rate [47].

In the unrotated state the stress/strain relationship is defined as,

$$\bar{\boldsymbol{\sigma}} = 2G\boldsymbol{\epsilon}_{dev}^e + 3K\boldsymbol{\epsilon}_{vol}^e, \quad (30)$$

where G is the shear modulus, K is the bulk modulus, $\boldsymbol{\epsilon}_{dev}^e$ is the deviatoric elastic strain and, $\boldsymbol{\epsilon}_{vol}^e$ is the volumetric elastic strain. The derivation of the material stress rate then easily follows,

$$\dot{\boldsymbol{\sigma}} = 2G\bar{\mathbf{d}}_{dev}^e + 3K\bar{\mathbf{d}}_{vol}^e, \quad (31)$$

where $\bar{\mathbf{d}}_{dev}^e$ is the deviatoric elastic strain rate and $\bar{\mathbf{d}}_{vol}^e$ is the volumetric elastic strain.

Due to the amorphous nature of the silicon in our investigation, the concentration dependent stress-free portion of strain may be regarded as isotropic and follows the same model used in [13]. This is analogous to the expressions used for isotropic thermal expansion [48],

$$\boldsymbol{\epsilon}^c = \eta(c - c_0)\mathbf{I}, \quad (32)$$

where η is the volume expansion coefficient and \mathbf{I} is the identity tensor. The material rate of stress-free volumetric strain is then,

$$\bar{\mathbf{d}}^c = \eta \frac{\partial c}{\partial t} \mathbf{I}. \quad (33)$$

3.3 Perfect Plasticity and Linear Strain Hardening

Two different plasticity models will be used to determine the rate of plastic strain, $\bar{\mathbf{d}}^p$. The first is perfect plasticity with the yield surfaces defined by,

$$\sqrt{\frac{3}{2}\bar{\boldsymbol{\sigma}}_{dev} : \bar{\boldsymbol{\sigma}}_{dev}} - \sigma_Y = 0, \quad (34)$$

and the second is linear isotropic strain hardening with the yield surface defined by,

$$\sqrt{\frac{3}{2}\bar{\boldsymbol{\sigma}}_{dev} : \bar{\boldsymbol{\sigma}}_{dev}} - (\sigma_Y + K\epsilon_{equiv}^p) = 0, \quad (35)$$

where σ_Y is the initial yield stress, $\bar{\boldsymbol{\sigma}}_{dev} = \bar{\boldsymbol{\sigma}} - 1/3tr(\bar{\boldsymbol{\sigma}})\mathbf{I}$ is the deviatoric stress, K is the plastic modulus, and ϵ_{equiv}^p is the equivalent plastic strain. A description of the method for computing $\bar{\mathbf{d}}^p$ is beyond the scope of this paper, but the interested reader is referred to [49] for a complete description of the algorithm. Both the perfectly plastic and linear isotropic strain hardening models are implemented within the Uintah MPM component [39] and are used for the simulations presented in this paper.

3.4 Stress Update

Using Equation 29, Equation 33, and the rate of plastic strain, $\bar{\mathbf{d}}^p$, the rate of elastic strain can then be calculated,

$$\bar{\mathbf{d}}^e = \bar{\mathbf{d}} - \bar{\mathbf{d}}^c - \bar{\mathbf{d}}^p. \quad (36)$$

The rate of elastic strain is then decomposed into its deviatoric and volumetric component,

$$\bar{\mathbf{d}}_{vol}^e = \frac{1}{3}tr(\bar{\mathbf{d}}^e)\mathbf{I}, \quad \bar{\mathbf{d}}_{dev}^e = \bar{\mathbf{d}}^e - \bar{\mathbf{d}}_{vol}^e. \quad (37)$$

Using the deviatoric and volumetric elastic strain rates the updated stress is then computed,

$$\bar{\boldsymbol{\sigma}}^{n+1} = \bar{\boldsymbol{\sigma}}^n + (2G\bar{\mathbf{d}}_{dev}^e + 3K\bar{\mathbf{d}}_{vol}^e)dt, \quad (38)$$

where $\bar{\boldsymbol{\sigma}}^n$ is the current stress, $\bar{\boldsymbol{\sigma}}^{n+1}$ is the updated stress, and dt is the timestep size. The last step in the stress update calculation is to rotate the updated stress to its rotated state,

$$\boldsymbol{\sigma}^{n+1} = \mathbf{R}\bar{\boldsymbol{\sigma}}^{n+1}\mathbf{R}^T. \quad (39)$$

4 Numerical Solution of the Model Problem

As was mentioned in the introduction, there have been a multitude of numerical simulations performed to study the effects of lithiation on silicon anodes. In these studies different anode geometries have been used. Three common choices have been a sphere, a nanowire, and a pillar. For the purposes of this paper the pillar geometry will be used and while the pillar geometry lends itself to a 2D axisymmetric numerical solution for the purposes of this paper full 3D simulations will be performed. Two different choices in pillar sizes will be used throughout this section. The smaller pillar has a diameter of $0.1 \mu m$ and a height of $0.1 \mu m$. The larger pillar has a diameter of $0.5 \mu m$ and a height of $0.05 \mu m$. Multiple simulations were run using the smaller pillar size to explore choices in constitutive model, parameter selection, and boundary conditions. With the results from the simulations performed using the smaller diameter pillar, decisions were then made as to constitutive model choice, parameter selection, and boundary conditions and then applied to simulations using the larger diameter pillar. The use of a substrate material was then explored using the larger diameter pillar.

4.1 Time Scales of Governing Equations

The governing equations for momentum balance and concentration diffusion are represented by Equation 1 and Equation 2. For the purposes of this paper the external forces acting on the nanopillar will be neglected, $\mathbf{b} = 0$, and Equation 1 can be reduced to,

$$\rho\mathbf{a} = \nabla \cdot \boldsymbol{\sigma}. \quad (40)$$

The time scales of these two different physical processes differ greatly in magnitude. As was discussed in Section 3.1 the range of values for diffusivity of lithium within amorphous silicon range between $10^{-17} m^2/s$ and $10^{-15} m^2/s$. On the other hand, the material response to changes in deformation happens at a much smaller time scale. The speed of sound within a given material is defined by the following equation,

$$c_s = \sqrt{\frac{K + 4/3G}{\rho}}, \quad (41)$$

where K is the bulk modulus, G is the shear modulus, and ρ is density. For amorphous silicon reasonable values for density, bulk modulus, and shear modulus are $2.33 \times 10^3 kg/m^3$, $67 GPa$, and $31 GPa$, respectively. Based on these values the sound speed for amorphous silicon is $6.8 \times 10^3 m/s$. A simple comparison of diffusivity and sound speed shows the large differences in time scale by which each of the physical processes occur. Because of this difference the momentum balance equation reaches a quasi-steady state,

$$\nabla \cdot \boldsymbol{\sigma} = 0, \quad (42)$$

within the time scale that diffusion occurs [16, 50, 51].

4.2 Time Integration and Time Step Selection

At the end of each iteration of the mpm algorithm a new time step, dt , is calculated. The size of the time step is limited by the numerical solutions for the diffusion equation and the momentum balance equation. The time step for the momentum balance equation is computed in the following manner,

$$dt_{mb} = \min \left(\frac{dx_{cell}}{c_s + v_x}, \frac{dy_{cell}}{c_s + v_y}, \frac{dz_{cell}}{c_s + v_z} \right), \quad (43)$$

where dx_{cell} , dy_{cell} , and dz_{cell} are the cell dimension and v_x , v_y , and v_z are the components of the particle velocity vector in the x , y , and z directions respectively.

The time step size based on the numerical solution for the diffusion equation is calculated as follows,

$$dt_{diff} = \min \left(\frac{dx_{cell}^2}{2D}, \frac{dy_{cell}^2}{2D}, \frac{dz_{cell}^2}{2D} \right), \quad (44)$$

where D is the diffusivity coefficient. The time step that is then used for the overall simulation is the smallest of the two time steps,

$$dt = \min(dt_{mb}, dt_{diff}). \quad (45)$$

4.2.1 Time Stepping Issues.

The time step criteria stated above is used to maintain a stable numerical solution, but if the time step needed for a stable solution becomes too small then computation time needed for a viable solution will become intractable. To illustrate this point, a stable time step is computed using Equation 43. The sound speed of $6.8 \times 10^3 m/s$ computed in Section 4.1 and a grid cell dimension of $dx_{cell} = 10^{-8} m$ is used in the calculation. For simplicity the particle velocity is neglected in the calculation because it small in comparison to the computed sound speed. The resulting time step is,

$$dt_{mb} = \frac{dx_{cell}}{c_s} = 6.8 \times 10^{-11} s. \quad (46)$$

Using the above computed time step size, 10^{11} time step integrations would be needed to reach 6.8s of simulation time. The number of time steps for this calculation would be intractable. By way of comparison, for a given diffusivity of $D = 10^{-15} m^2/s$ the calculated time step size is,

$$dt_{diff} = \frac{dx_{cell}^2}{2D} = 0.05s, \quad (47)$$

which is a tractable time step size.

From the above example it can be seen that for a simulation to run in a reasonable time a stable means of increasing dt_{mb} to a tractable time step size needs to be found. Ideally the time step size would be limited by the diffusion calculations and not momentum balance.

In order to increase the limiting time step size needed for the numerical solution to the momentum balance equation, the density of silicon is artificially raised to a value such that the limiting time step criteria is dependent upon the numerical solution of the diffusion equation and not the solution to the momentum balance equation. The argument for the validity of artificially raising the density stems from the observations made in Section 4.1 that within the time scale of chemical diffusion the momentum balance equation reaches a quasi-static state. Using constitutive relationship found in Equation 30, Equation 40 can be rewritten as,

$$\rho \mathbf{a} = 2G \nabla \cdot \boldsymbol{\epsilon}_{dev}^e + 3K \nabla \cdot \boldsymbol{\epsilon}_{vol}^e, \quad (48)$$

and dividing through by density produces the equation for acceleration,

$$\mathbf{a} = \frac{2G}{\rho} \nabla \cdot \boldsymbol{\epsilon}_{dev}^e + \frac{3K}{\rho} \nabla \cdot \boldsymbol{\epsilon}_{vol}^e. \quad (49)$$

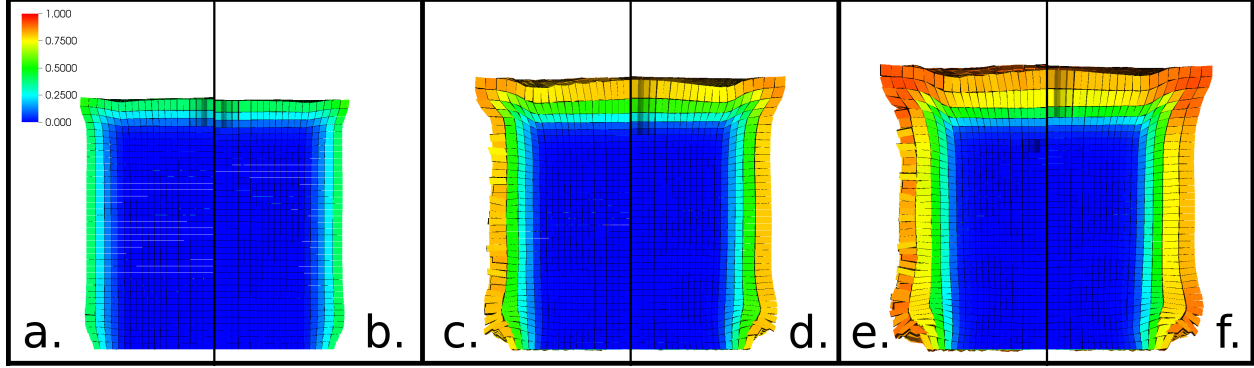


Figure 3: (a,c,e) density of $2.33 \times 10^3 \text{ kg/m}^3$ and (b,c,f) density of $2.33 \times 10^8 \text{ kg/m}^3$

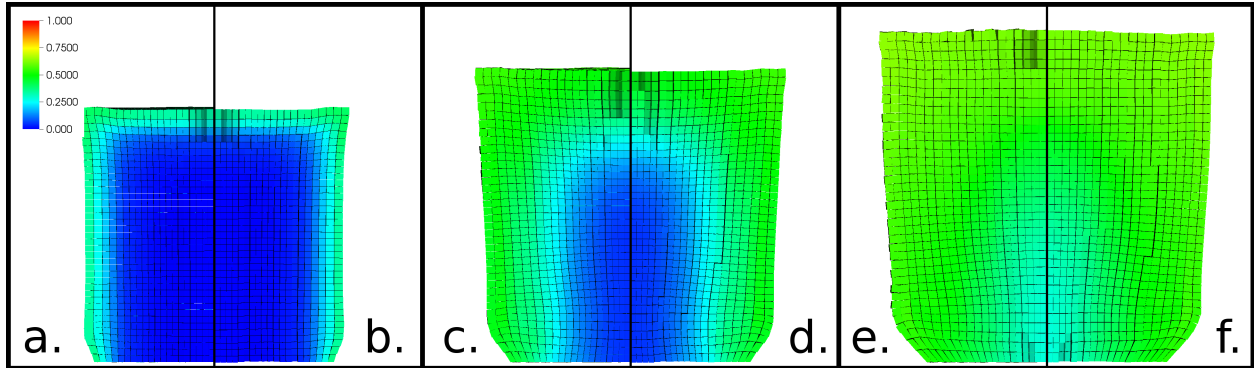


Figure 4: (a,c,e) density of $2.33 \times 10^{18} \text{ kg/m}^3$ and (b,c,f) density of $2.33 \times 10^{24} \text{ kg/m}^3$

An increase in density decreases the speed by which elastic waves travel through the material, but the elastic strain remains the same.

For the purposes of demonstration, two different sets of numerical simulations were run. In the first set of numerical experiments two simulations were run. In the first simulation the density for amorphous silicon is used, $2.33 \times 10^3 \text{ kg/m}^3$. The bulk and shear moduli are 67 GPa and 31 GPa , respectively. The linear isotropic strain hardening constitutive model is used with a yield stress of 1.4 GPa and a plastic modulus of 1.15 GPa . The initial diffusivity is artificially increased to $D_0 = 10^{-10} \text{ m}^2/\text{s}$. In the second simulation the density is increased to $2.33 \times 10^8 \text{ kg/m}^3$ with all other parameters remaining the same. Figure 3 shows a side by side comparison of the two simulations at $6.0 \times 10^{-9} \text{ s}$, $26.0 \times 10^{-9} \text{ s}$, and $48.0 \times 10^{-9} \text{ s}$. From Figure 3 it can be seen that even with a five order increase in density, qualitatively the variations between the simulations are small.

In the second set of simulations two simulations were run. In the first, an initial diffusivity is set to $D_0 = 10^{-17} \text{ m}^2/\text{s}$, which falls within the range of published values [52]. The density is artificially raised to $2.33 \times 10^{18} \text{ kg/m}^3$. The bulk and shear moduli are 67 GPa and 31 GPa , respectively. The linear isotropic strain hardening constitutive model is used with a yield stress of 1.4 GPa and a plastic modulus of 1.15 GPa . The second test was run using an initial density of $2.33 \times 10^{24} \text{ kg/m}^3$. Figure 4 shows a side by side comparison of the two simulations at three different time steps - 4.0 s , 16.0 s , and 28.0 s . From Figure 4 it can be seen qualitatively that there is very little variation between the two simulations despite the five orders of magnitude difference in density.

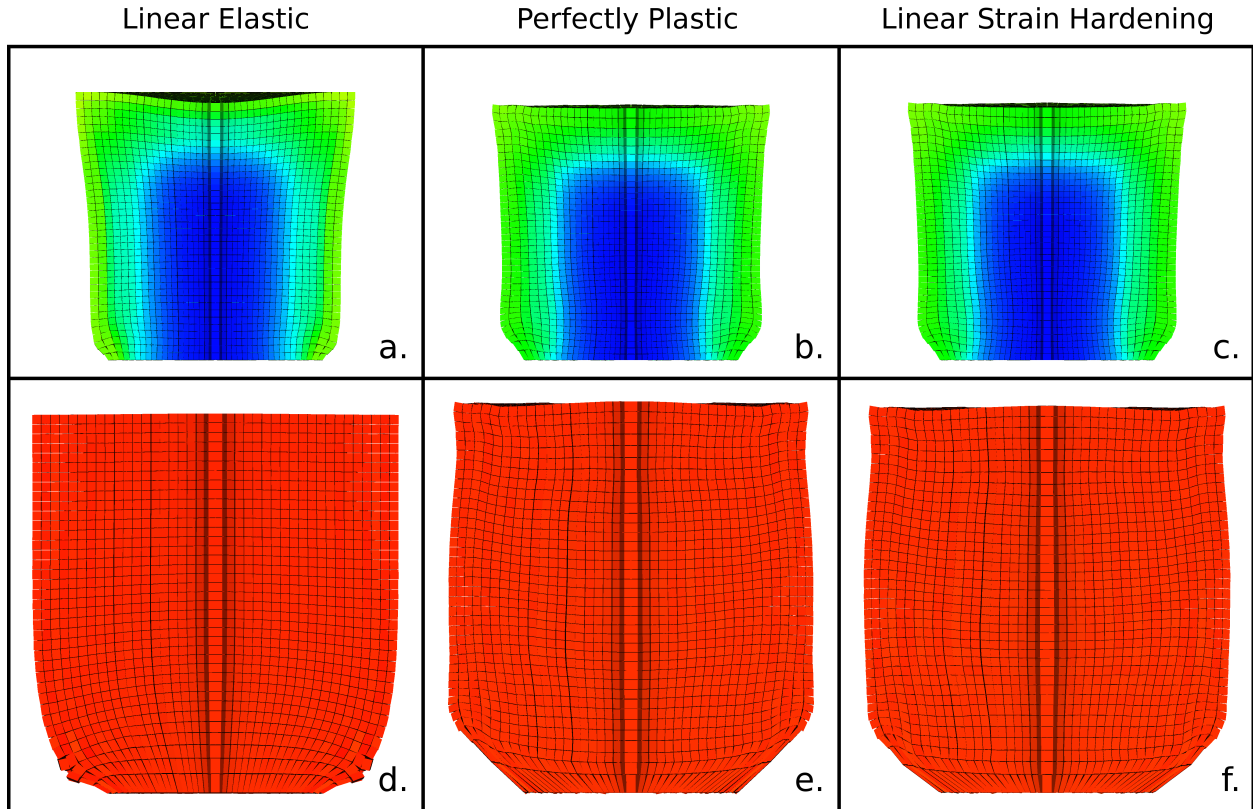


Figure 5: Fig.(a-c) are images of pillars mid-saturation and Fig.(d-f) are images of pillars at full-saturation. Fig.(a,d) Linear Elastic, Fig.(b,e) Perfect Plasticity, Fig.(c,f) Linear Strain Hardening.

4.3 Comparison of Constitutive Models

A proper constitutive model needs to be selected in order to achieve the desired behavior that matches that of a silicon anode during lithiation. Simulations were run using three different constitutive models, linear elastic, perfectly plastic, and linear isotropic strain hardening. The bulk and shear moduli for all three models are 67 GPa and 31 GPa , respectively. For the perfectly plastic and linear isotropic strain models the yield stress is 1.4 GPa and for the linear isotropic strain hardening models the plastic modulus is 1.15 GPa . The volume expansion coefficient used for this set of simulations and all subsequent simulations is $\eta = .56$. The flux boundary conditions and diffusivity parameters are the same for all three simulations.

Figure 5 shows images of the pillars at mid-saturation and full saturation. From the image it can be seen that at full saturation there is a noticeable difference between the linear elastic and the two plasticity models. The largest noticeable difference is along the base of the pillars where the largest concentration of plastic deformation occurs. In images (a-c) of Figure 5 it can be seen that plastic deformation is already occurring along the base of the pillars producing different deformation patterns compared against the linear elastic pillar.

While there are noticeable differences between the linear elastic model and the two plasticity models there are also qualitative differences between the two plasticity models.

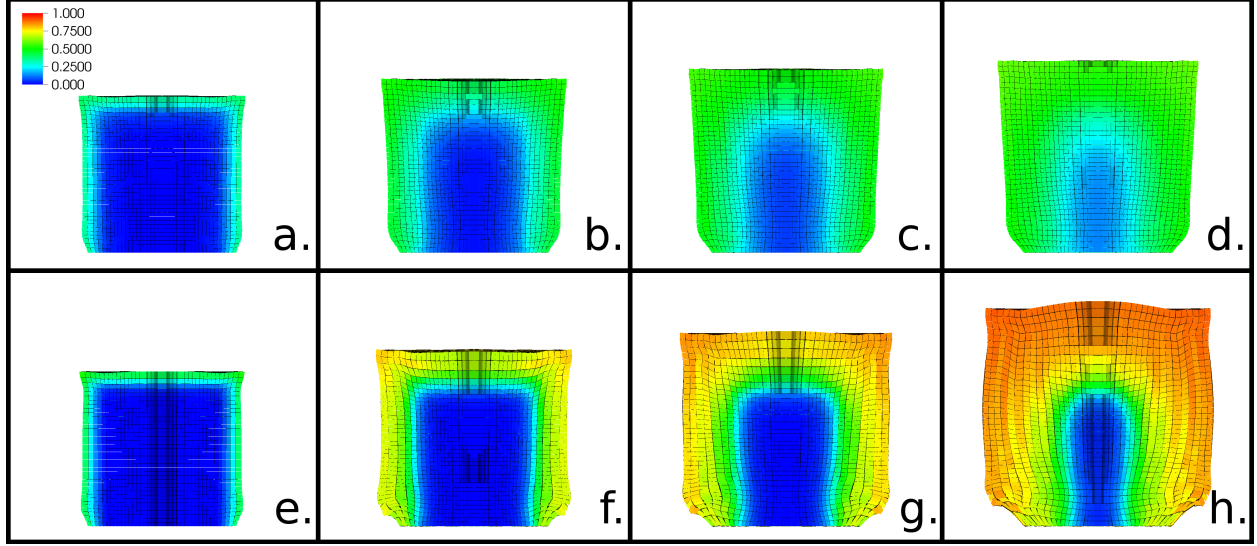


Figure 6: (a-d) series of images during the lithiation process using a 10^{-9} flux boundary condition and the linear isotropic strain hardening model. (e-h) series of images during the lithiation process using a 10^{-8} flux boundary condition and the linear isotropic strain hardening model.

4.4 Affects of Flux Boundary Conditions

Both the perfectly plastic and the linear strain hardening constitutive models are dependent upon the prior history of the material. Because of this history dependent behavior the choice of flux boundary conditions affects the shape of the pillars. To demonstrate the affect that the choice of the flux magnitude has on deformation behavior two different simulations were run. The diffusion parameters for both simulations are $\alpha = 6$, $\beta = 0.5$, and $p_{max} = 3 \text{ GPa}$. The linear isotropic strain hardening constitutive model is used with the bulk and shear modulus values of 67 GPa and 31 GPa , respectively. The yield stress is 1.4 GPa and the plasticity modulus is 1.15 GPa . The magnitude of the flux boundary condition are 10^{-9} and 10^{-8} . Figure 6 shows two sequence of images where the top row shows results from the simulation run at the lower flux value and the lower row shows the sequence of images for the simulation run at the higher flux value.

Both sets of simulations illustrate the sharp transition between high normalized concentrations and low normalized concentrations as the lithium diffuses through the anode. The noticeable difference between the simulations is in the normalized concentration levels that are behind the sharp transition in normalized concentration. As would be expected the simulation with the larger influx of normalized concentration will have larger normalized concentration values behind the high/low transition. From the experimental results presented by Wang et al. the initial concentration values behind the phase transition have a normalized concentration of ~ 0.67 . For the lower flux boundary condition the normalized concentration values fall in the range of 0.5 to 0.6 while the high flux boundary condition have normalized concentration values greater than 0.7.

As can be seen from Figure 6, differences in flux boundary condition values not only affects the level of concentration values behind the sharp phase transition it also changes patterns in deformation. In the pillar with the larger flux boundary condition values the bulging near the base is more pronounced in comparison to the pillar with the small flux values. Figure 7 shows the state of the the nanopillar as it reaches its fully lithiated state where the differences in flux boundary condition values produces noticeable differences in the deformation of the nanopillar.

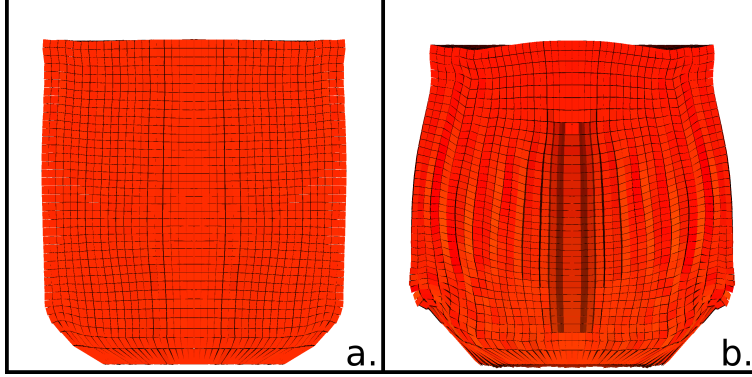


Figure 7: (a) fully lithiated state of nanopillar using 10^{-9} flux boundary condition and the linear isotropic strain hardening model. (b) fully lithiated state of nanopillar using 10^{-8} flux boundary condition and the linear isotropic strain hardening model.

4.5 Diffusivity

Using density functional theory calculations a range of diffusivity values have been determined for diffusion of lithiation in amorphous silicon of $10^{-18}\text{m}^2\text{s}^{-1}$ to $10^{-14}\text{m}^2\text{s}^{-1}$ [52]. The diffusivity model presented in this paper produces diffusivity values that fall within the proposed range. The issue that has been discovered is that while the calculated values for diffusivity may fall within the computed range of values for a chosen set of tuning parameters, the deformation behavior can vary based on what tuning parameters are chosen.

Previous works [5, 19, 20, 21] have chosen models that compute diffusivity solely as a function of concentration. But it's clear that the mobility of lithium ions within amorphous silicon has to be a function of both lithium concentrations and pressure. From numerical experiments it can be seen that the inclusion of pressure in the diffusivity calculation does affect the deformation of the pillar during lithiation.

Two simulations were run to show the difference that can occur when pressure is accounted for in the diffusivity calculation. The first simulation used the following parameters, $\alpha = 6.0$ and $\beta = 0.0$, and the second simulation used $\alpha = 6.0$ and $\beta = 1.0$. By setting β equal to zero, pressure is neglected from the calculation. Both simulations used the linear isotropic strain hardening constitutive model with bulk and shear modulus values of 67 GPa and 31 GPa , respectively. The yield stress is 1.4 GPa and the plasticity modulus is 1.15 GPa . The magnitude of the flux boundary condition is 10^{-9} . Figure 8 shows a comparison of the two simulation. Figure 8.a and Figure 8.b show the results of the simulation during the lithiation process, from these figures it can be seen that by changing the pressure tuning parameter the difference in deformations, especially near the base of the pillar, are noticeable. Figure 8.c and Figure 8.d show the results of the simulations as the pillars reach full saturation. In the fully lithiated state the differences between the two simulations are less noticeable. Both sets of parameters produce the sharp phase transition between high and low normalized concentration levels as lithium diffuses through the pillar. The difference being in the deformation behavior during the lithiation process.

4.6 Use of Material Substrate

Up to this point all simulations have been made with the assumption that the base of the pillar is fixed. Experimental results show that this is not the case. Wang et al. [5] have shown through experiments that the base of the electrode can expand in the radial direction by $\sim 20\%$. It is unknown if the deformation comes as a result of the sliding between the anode and the substrate material or deformation in the substrate.

Two simulations were run to test the effects that a deformable material substrate will have on pillar deformation. For the purposes of this paper the pillar is assumed to be affixed to the substrate and the substrate material is allowed to deform. The bulk and shear moduli of the substrate material are 180.4 GPa and 76 GPa , respectively. The density of the material is the same as that of the pillar. The linear isotropic

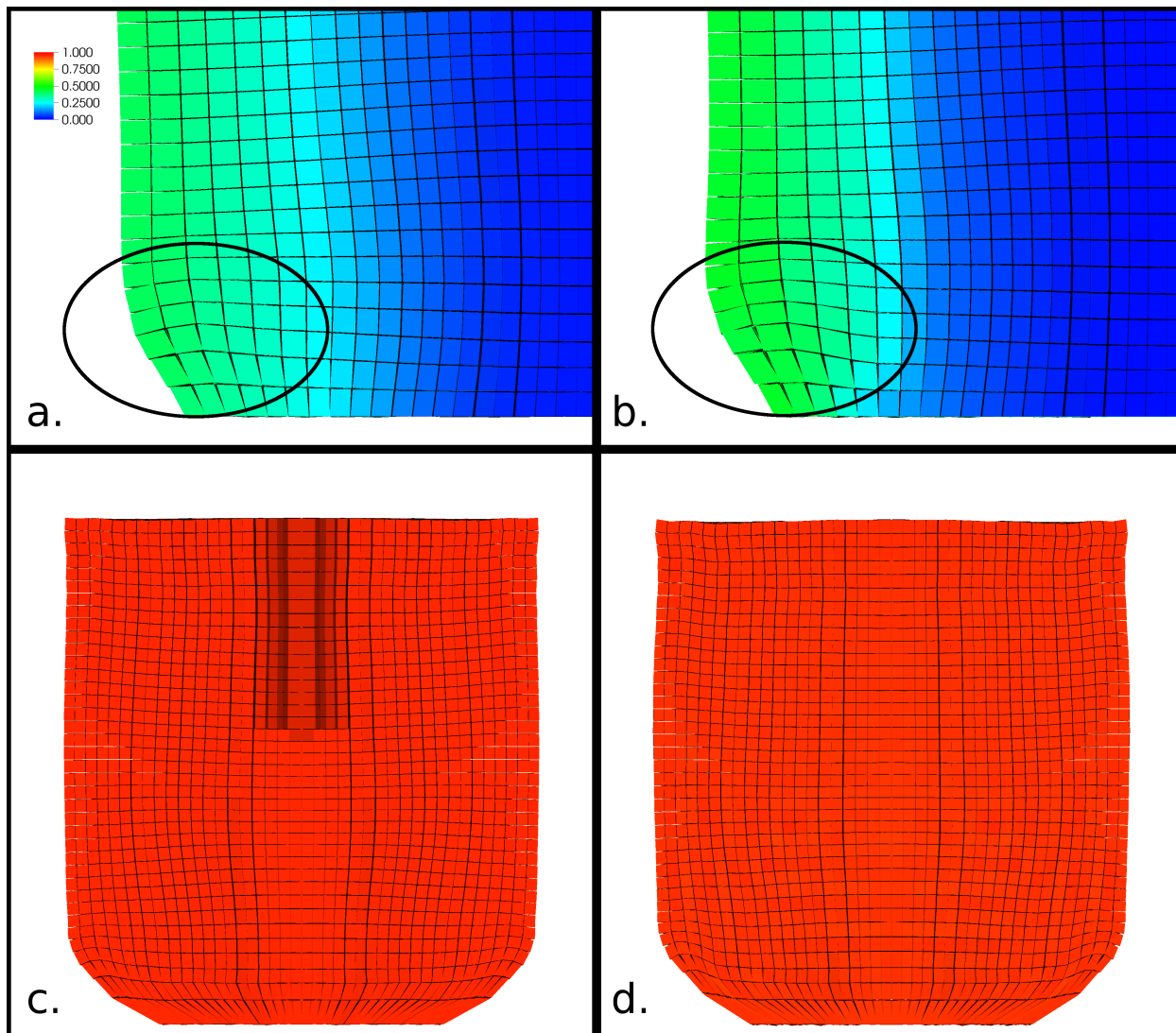


Figure 8: (a) pillar using diffusivity parameters $\alpha = 6.0$ and $\beta = 0.0$ during lithiation process. (b) pillar using diffusivity parameters $\alpha = 6.0$ and $\beta = 1.0$ during lithiation process. (c) pillar using diffusivity parameters $\alpha = 6.0$ and $\beta = 0.0$ at full saturation. (d) pillar using diffusivity parameters $\alpha = 6.0$ and $\beta = 1.0$ at full saturation.

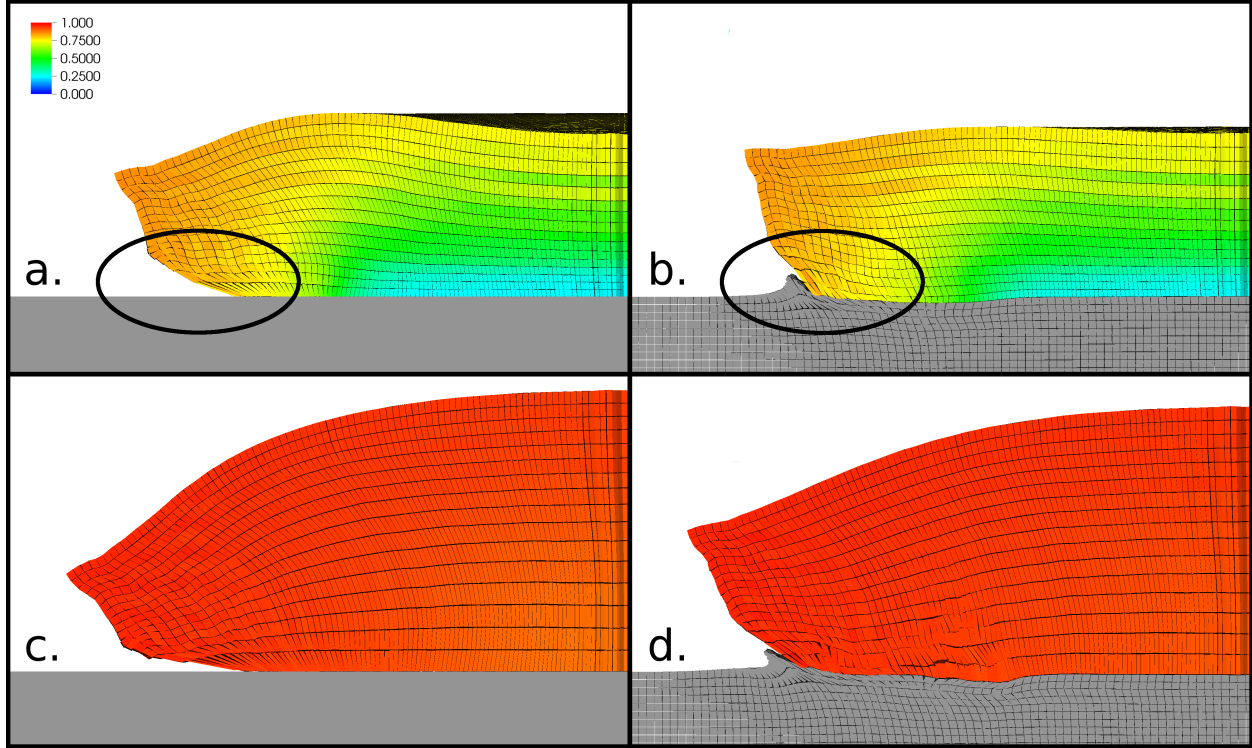


Figure 9: (a,c) pillar attached to a non-deformable material substrate. (b,d) pillar attached to a deformable material substrate

strain hardening plasticity model is used with a yield stress of $.7\text{ GPa}$ and a plasticity modulus of 1.15 GPa . Figure 9 shows a comparison between the pillar attached to a non deformable substrate and a pillar attached to a deformable substrate.

From Figure 9 it can be seen that there are noticeable differences between the two simulations. In the non-deformable substrate image it can be seen that large deformations occur in the region where pillar attaches to the base, by way of comparison in the deformable substrate image it can be seen that the deformation due to the pillar swelling is shared between both the pillar and the substrate. The deformable substrate reduces the acute deformations that occur in the pillar as highlighted by circled regions of Figure 9.a and Figure 9.b.

The use of a deformable substrate also affects the shape of the pillar as it reaches full lithiation. Figure 9.c and Figure 9.d show the pillars in the lithiated state. A visual comparison of the images shows that the shapes of the two pillars are different.

4.7 The Full Lithiation and Delithiation Cycle of the Silicon Anode

Using what was learned from the previous sections a full lithiation/delithiation cycle was performed on the large pillar. The linear isotropic strain hardening constitutive model was used for the pillar with the bulk and shear moduli being 67.0 GPa and 31.0 GPa , respectively, the yield stress was 1.4 GPa and the plasticity modulus was 1.15 GPa . The diffusivity parameters used during the lithiation phase were $D_0 = 10^{-17}\text{ m}^2/\text{s}$, $\alpha = 6.0$, $\beta = 0.5$ and $p_{max} = 3\text{ GPa}$. During the delithiation phase diffusivity was fixed at the final diffusivity value during the lithation phase. The linear isotropic strain hardening constitutive model was used for the substrate material with the bulk and shear moduli being 180.4 GPa and 76.0 GPa , respectively, the yield stress was 0.7 GPa and the plasticity modulus was 1.15 GPa . There was no diffusion of lithium into the substrate material. Figure 10 shows the results from the simulation of the silicon anode undergoing the full

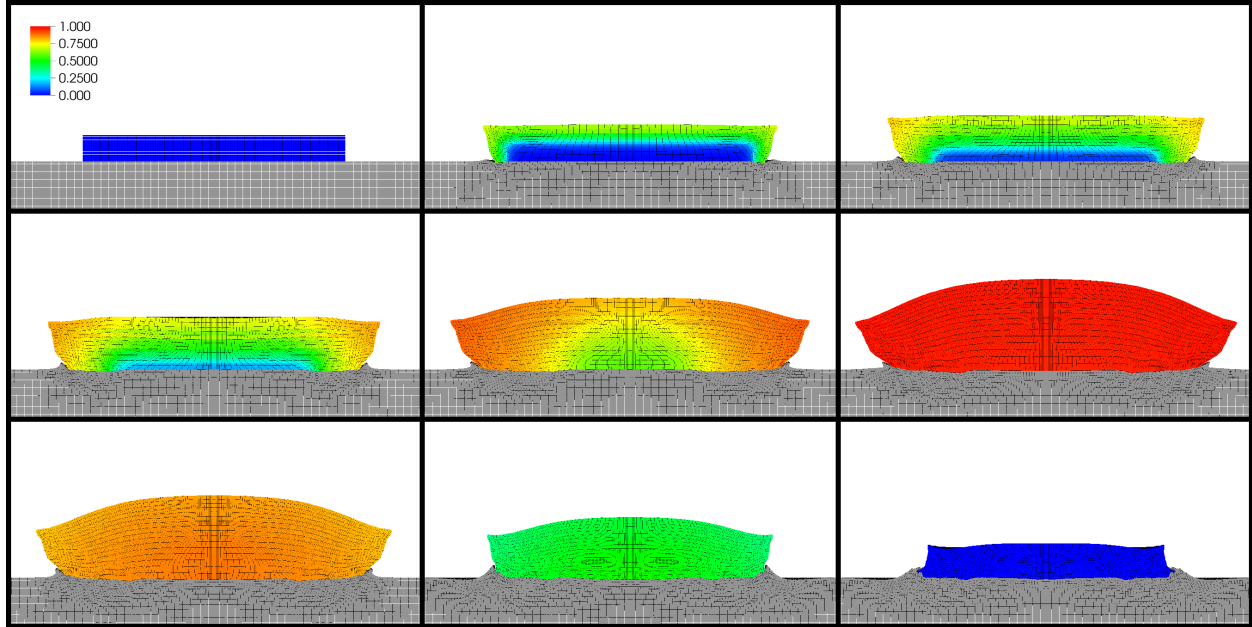


Figure 10: A sequence of images showing the full lithiation and delithiation of a silicon nanopillar.

lithiation/delithiation cycle.

As was discussed in the introduction to this paper and by Wang et. al. [5] one key observable trait of the lithiation of silicon is the sharp lithiation front that occurs during the lithiation process. As can be seen from Figure 10 the sharp lithiation front is present during the lithiation phase of the simulation. Another key observable trait found in both the simulation and in experiments [5] is the occurrence of the much more shallow concentration gradients in the region behind the sharp lithiation front.

For the delithiation phase of the simulation the diffusivity value was fixed at last value obtained during the lithiation phase. With the use of the fixed larger diffusivity value the rate of diffusion throughout the entire pillar appears to be more uniform. A comparison of the first and last images of the sequence found in Figure 10 shows the amount of plastic deformation that occurs in both the nanopillar and the substrate during one full lithiation/delithiation cycle.

The simulation was run on 9 cores of a single compute node. The cpu for the compute node is an Intel Xeon E5-2667 with 6 physical cores extended to 12 cores with hyper-threading enabled. The cpu clock speed is 2.9GHz. The total number of time steps needed to complete the simulation was 27472 and the estimated wall-clock time was 48.57 hours.

5 Conclusion

Silicon has the ability to absorb up to 3.75 lithium ions for each silicon atom. The ability to absorb large amounts of lithium make silicon an excellent candidate material to increase the efficiency of electrochemical storage devices. The drawbacks for silicon is the accompanying large volume change that comes as a result of absorbing large amounts of lithium. The ability to simulate accurately the large physical deformations that occur during the lithiation/delithiation of silicon will to help to better how it can best be used as an anode material.

In this paper it has been demonstrated that the full lithiation and delithiation of a silicon anode can be simulated using the Material Point Method. A description of the method for used to model diffusion within MPM was given and validation tests were performed. This paper presented a coupled chemical-mechanical

model that couples stress to the diffusion process and concentration to the constitutive model for stress. The coupled chemical-mechanical model was implemented in the Uintah Computational Framework's MPM component. Multiple numerical simulations were run to explore the different possible choices that could be made pertaining to constitutive model selection, boundary conditions, and parameter selection. Using what was learned from the different numerical simulations a full lithiation/delithiation cycle simulation was performed.

The implementation of the coupled chemical-mechanical model into the Uintah Computational Framework allows for Uintah MPM to be used as a tool to for future work in examining different anode geometries, material substrates, and flux rates.

In future work methods for modeling fracture need to be introduced into the Uintah framework in order to better simulate the full physical effects of lithiation and delithiation on a silicon anode. In this current work the affects of an applied voltage have been approximated using the flux boundary condition. Future work needs to be done to implement the full electrochemistry in to the numerical models.

Acknowledgement

This research was primarily sponsored by the Army Research Laboratory and was accomplished under Cooperative Agreement Number W911NF-12-2-0023. The views and conclusions contained in this document are those of the authors and should not be interpreted as representing the official policies, either expressed or implied, of the Army Research Laboratory or the U.S. Government.

This is an author-created, un-copyedited version of an article accepted for publication/published in *Modelling and Simulation in Materials Science and Engineering*. IOP Publishing Ltd is not responsible for any errors or omissions in this version of the manuscript or any version derived from it. The Version of Record is available online at <https://doi.org/10.1088/1361-651X/aa6830>.

References

- [1] M. N. Obrovac and Leif Christensen. Structural changes in silicon anodes during lithium insertion/extraction. *Electrochemical and Solid-State Letters*, 7(5):A93–A96, 2004.
- [2] C.K. Chan, H. Peng, G. Liu, K. McIlwrath, X.F. Zhang, R.A. Huggins, and Y. Cui. High-performance lithium battery anodes using silicon nanowires. *Nature Nanotechnology*, 3(1):31–35, 2008.
- [3] J.M. Tarascon and M. Armand. Issues and challenges facing rechargeable lithium batteries. *Nature*, 414(6861):359–367, 2001.
- [4] V. A. Sethuraman, V. Srinivasan, A. F. Bower, and P. R. Guduru. In situ measurements of stress-potential coupling in lithiated silicon. *Journal of The Electrochemical Society*, 157(11):A1253–A1261, 2010.
- [5] Jiang Wei Wang, Yu He, Feifei Fan, Xiao Hua Liu, Shuman Xia, Yang Liu, C. Thomas Harris, Hong Li, Jian Yu Huang, Scott X. Mao, and Ting Zhu. Two-phase electrochemical lithiation in amorphous silicon. *Nano Letters*, 13(2):709–715, 2013.
- [6] Shigeaki Ohara, Junji Suzuki, Kyoichi Sekine, and Tsutomu Takamura. A thin film silicon anode for li-ion batteries having a very large specific capacity and long cycle life. *Journal of Power Sources*, 136(2):303 – 306, 2004. Selected papers presented at the International Power Sources Symposium.

- [7] Eric Mills, John Cannarella, Qi Zhang, Shoham Bhadra, Craig B. Arnold, and Stephen Y. Chou. Silicon nanopillar anodes for lithium-ion batteries using nanoimprint lithography with flexible molds. *Journal of Vacuum Science and Technology B*, 32(6), 2014.
- [8] Loc Baggetto, Dmitry Danilov, and Peter H. L. Notten. Honeycomb-structured silicon: Remarkable morphological changes induced by electrochemical (de)lithiation. *Advanced Materials*, 23(13):1563–1566, 2011.
- [9] S. Prussin. Generation and distribution of dislocations by solute diffusion. *Journal of Applied Physics*, 32(10):1876–1881, 1961.
- [10] J.C.M. Li, R.A. Oriani, and L.S. Darken. The thermodynamics of stressed solids. *Zeitschrift für Physikalische Chemie*, 49:271–290, 1966.
- [11] F Larché and J.W Cahn. A linear theory of thermochemical equilibrium of solids under stress. *Acta Metallurgica*, 21(8):1051 – 1063, 1973.
- [12] Francis Larché and John W. Cahn. A nonlinear theory of thermochemical equilibrium of solids under stress. *Acta Metallurgica*, 26(1):53 – 60, 1978.
- [13] F.C. Larché and J.I. Cahn. The effect of self-stress on diffusion in solids. *Acta Metallurgica*, 30(10):1835 – 1845, 1982.
- [14] F.C. Larché and J.W. Cahn. Overview no. 41 the interactions of composition and stress in crystalline solids. *Acta Metallurgica*, 33(3):331 – 357, 1985.
- [15] A.F. Bower, P.R. Guduru, and V.A. Sethuraman. A finite strain model of stress, diffusion, plastic flow, and electrochemical reactions in a lithium-ion half-cell. *Journal of the Mechanics and Physics of Solids*, 59(4):804 – 828, 2011.
- [16] Yi-Fan Gao and Min Zhou. Strong dependency of lithium diffusion on mechanical constraints in high-capacity li-ion battery electrodes. *Acta Mechanica Sinica*, 28(4):1068–1077, 2012.
- [17] Chien H. Wu. The role of eshelby stress in composition-generated and stress-assisted diffusion. *Journal of the Mechanics and Physics of Solids*, 49(8):1771 – 1794, 2001.
- [18] Zhiwei Cui, Feng Gao, and Jianmin Qu. A finite deformation stress-dependent chemical potential and its applications to lithium ion batteries. *Journal of the Mechanics and Physics of Solids*, 60(7):1280 – 1295, 2012.
- [19] Xiao Hua Liu, Li Zhong, Shan Huang, Scott X. Mao, Ting Zhu, and Jian Yu Huang. Size-dependent fracture of silicon nanoparticles during lithiation. *ACS Nano*, 6(2):1522–1531, 2012. PMID: 22217200.
- [20] Miao Wang, Xinran Xiao, and Xiaosong Huang. Study of lithium diffusivity in amorphous silicon via finite element analysis. *Journal of Power Sources*, 307:77 – 85, 2016.
- [21] Lucas A. Berla, Seok Woo Lee, Ill Ryu, Yi Cui, and William D. Nix. Robustness of amorphous silicon during the initial lithiation/delithiation cycle. *Journal of Power Sources*, 258:253 – 259, 2014.
- [22] John Christensen and John Newman. Stress generation and fracture in lithium insertion materials. *Journal of Solid State Electrochemistry*, 10(5):293–319, 2006.
- [23] A.D. Drozdov. Viscoplastic response of electrode particles in li-ion batteries driven by insertion of lithium. *International Journal of Solids and Structures*, 51(34):690 – 705, 2014.
- [24] Yonghao An and Hanqing Jiang. A finite element simulation on transient large deformation and mass diffusion in electrodes for lithium ion batteries. *Modelling and Simulation in Materials Science and Engineering*, 21(7):074007, 2013.

- [25] Xiao Hua Liu, He Zheng, Li Zhong, Shan Huang, Khim Karki, Li Qiang Zhang, Yang Liu, Akihiro Kushima, Wen Tao Liang, Jiang Wei Wang, Jeong-Hyun Cho, Eric Epstein, Shadi A. Dayeh, S. Tom Picraux, Ting Zhu, Ju Li, John P. Sullivan, John Cumings, Chunsheng Wang, Scott X. Mao, Zhi Zhen Ye, Sulin Zhang, and Jian Yu Huang. Anisotropic swelling and fracture of silicon nanowires during lithiation. *Nano Letters*, 11(8):3312–3318, 2011. PMID: 21707052.
- [26] A F Bower and P R Guduru. A simple finite element model of diffusion, finite deformation, plasticity and fracture in lithium ion insertion electrode materials. *Modelling and Simulation in Materials Science and Engineering*, 20(4):045004, 2012.
- [27] G. Irving, J. Teran, and R. Fedkiw. Invertible finite elements for robust simulation of large deformation. In *Proceedings of the 2004 ACM SIGGRAPH/Eurographics Symposium on Computer Animation, SCA '04*, pages 131–140, Aire-la-Ville, Switzerland, Switzerland, 2004. Eurographics Association.
- [28] M. Anahid and A. R. Khoei. New development in extended finite element modeling of large elasto-plastic deformations. *International Journal for Numerical Methods in Engineering*, 75(10):1133–1171, 2008.
- [29] Chong Peng, Wei Wu, Hai-sui Yu, and Chun Wang. A sph approach for large deformation analysis with hypoplastic constitutive model. *Acta Geotechnica*, 10(6):703–717, 2015.
- [30] J.-S. Chen, C. Pan, and C.-T. Wu. Large deformation analysis of rubber based on a reproducing kernel particle method. *Computational Mechanics*, 19(3):211–227, 1997.
- [31] S.G. Bardenhagen, A.D. Brydon, and J.E. Guilkey. Insight into the physics of foam densification via numerical simulation. *Journal of the Mechanics and Physics of Solids*, 53(3):597 – 617, 2005.
- [32] D. Sulsky, Z. Chen, and H.L. Schreyer. A particle method for history-dependent materials. *Computer Methods in Applied Mechanics and Engineering*, 118(1):179 – 196, 1994.
- [33] Deborah Sulsky, Shi-Jian Zhou, and Howard L. Schreyer. Application of a particle-in-cell method to solid mechanics. *Computer Physics Communications*, 87(12):236 – 252, 1995. Particle Simulation Methods.
- [34] M. Steffen, P.C. Wallstedt, J.E. Guilkey, R.M. Kirby, and M. Berzins. Examination and analysis of implementation choices within the material point method (MPM). *Computer Modeling in Engineering & Sciences*, 31(2):107–127, 2008.
- [35] M. Steffen, R.M. Kirby, and M. Berzins. Analysis and reduction of quadrature errors in the material point method (MPM). *International Journal for Numerical Methods in Engineering*, 76(6):922–948, 2008.
- [36] M. Steffen, R.M. Kirby, and M. Berzins. Decoupling and balancing of space and time errors in the material point method (mpm). *International Journal for Numerical Methods in Engineering*, 82(10):1207–1243, 2010.
- [37] SG Bardenhagen and EM Kober. The generalized interpolation material point method. *Computer Modeling in Engineering and Sciences*, 5(6):477–496, 2004.
- [38] A. Sadeghirad, R. M. Brannon, and J. Burghardt. A convected particle domain interpolation technique to extend applicability of the material point method for problems involving massive deformations. *International Journal for Numerical Methods in Engineering*, 86(12):1435–1456, 2011.
- [39] Uintah computational framework. <http://uintah.utah.edu/>.
- [40] Uintah user guide. <http://uintah-build.sci.utah.edu/trac/wiki/Documentation/>.
- [41] John A. Nairn and James E. Guilkey. Axisymmetric form of the generalized interpolation material point method. *International Journal for Numerical Methods in Engineering*, 101(2):127–147, 2015.

- [42] X.Y. Gu, C.Y. Dong, T. Cheng, Y. Zhang, and Y. Bai. The transient heat conduction {MPM} and {GIMP} applied to isotropic materials. *Engineering Analysis with Boundary Elements*, 66:155 – 167, 2016.
- [43] Timothy Fagan, Vincent Lemiale, John Nairn, Yogita Ahuja, Raafat Ibrahim, and Yuri Estrin. Detailed thermal and material flow analyses of friction stir forming using a three-dimensional particle based model. *Journal of Materials Processing Technology*, 231:422 – 430, 2016.
- [44] J. David Logan. *Applied Partial Differential Equations*. Springer, 2nd edition, 2013.
- [45] Y. F. Gao and M. Zhou. Strong stress-enhanced diffusion in amorphous lithium alloy nanowire electrodes. *Journal of Applied Physics*, 109(1), 2011.
- [46] Laurence Brassart and Zhigang Suo. Reactive flow in large-deformation electrodes of lithium-ion batteries. *International Journal of Applied Mechanics*, 04(03):1250023, 2012.
- [47] R. M. Brannon. personal communication.
- [48] Gerhard A. Holzapfel. *Nonlinear Solid Mechanics, A Continuum Approach for Engineering*. John Wiley and Sons Ltd, The Atrium, Southern Gate, Chichester, West Sussex PO19 8SQ, England, 2006.
- [49] J.C Simo and T.J.R. Hughes. *Computational Inelasticity*, volume 7. Springer-Verlag New York, 1998.
- [50] Hui Yang, Feifei Fan, Wentao Liang, Xu Guo, Ting Zhu, and Sulin Zhang. A chemo-mechanical model of lithiation in silicon. *Journal of the Mechanics and Physics of Solids*, 70:349 – 361, 2014.
- [51] Sulin Zhang. Chemomechanical modeling of lithiation-induced failure in high-volume-change electrode materials for lithium ion batteries. *npj Computational Materials*, 3, 2017.
- [52] Georgios A. Tritsarlis, Kejie Zhao, Onyekwelu U. Okeke, and Efthimios Kaxiras. Diffusion of lithium in bulk amorphous silicon: A theoretical study. *The Journal of Physical Chemistry C*, 116(42):22212–22216, 2012.